GIGAHERTZ SCANNING ELECTRON ACOUSTIC MICROSCOPY

A Thesis

Presented to the Faculty of the Graduate School

of Cornell University

in Partial Fulfillment of the Requirements for the Degree of

Master of Science

by

Di Ni

August 2017

ABSTRACT

In Scanning Electron Acoustic Microscopy (SEAM) an electron beam with the beam current impacting a target site is modulated at acoustic or ultrasonic frequencies. The absorbed energy of the electrons results in a time-varying thermal expansion that leads to acoustic and ultrasonic waves to be launched into the substrate. The waves are detected using a piezoelectric transducer. As the electron beam is scanned, SEAM produces images that are indicative of the target thermal properties and ultrasonic wave properties.

SEAM has been shown to produce images that are useful in characterizing thermal and elastic properties, in the MHz frequency range. The main contrast mechanism is understood to be due to heat induced acoustic waves. The resolution of SEAM imaging is determined by the thermal generation volume, which is a function of the electron beam energy, electron beam focus diameter, thermal diffusion lengths, and the ultrasonic wavelength. The research presented in this thesis is motivated to extend the SEAM technique to the gigahertz range in order to realize nanometer scale SEAM resolution. Gigahertz SEAM uses a gigahertz modulated electron beam to generate a thermal acoustic wave and uses a piezoelectric thin film of aluminum-nitride (AlN) as the transducer. The resonance frequency of the AlN transducer is in the 1-2GHz range, enabling the GHz-SEAM to be investigated.

In this thesis, the theoretical model for the generating acoustic wave is developed as a function of the electron beam modulation frequency. This model demonstrates the potential to reach 10-100nm resolution with GHz-SEAM. SEAM is validated with an electron beam modulated using an electrostatic par-

allel plate deflector, at both MHz and GHz frequencies. PZT transducers are used at MHz frequencies and the measured output voltages on the transducers agree with theory. AlN transducers are used to sense the SEAM signals at GHz modulation. The signal amplitude suffers from considerable RF coupling, although data suggest that we can observe GHz-SEAM signals. The thesis proposes new measurement approaches to increase the SNR in GHz SEAM experiments in the future.

BIOGRAPHICAL SKETCH

Di Ni was born in Zhengzhou, Henan, China. She attended Zhengzhou No.1 High School and graduated in 2011. She earned the Bachelor of Science degree in Physics from Beijing Normal University, China in 2015. She came to Cornell University and obtained the Master of Science degree in Applied Physics. She joined the SonicMEMS Lab in 2016 conducting research in Scanning Electron Acoustic Microscopy, where she will continue pursuing her Ph.D.

To my parents

ACKNOWLEDGEMENTS

I would like thank my advisor Professor Amit Lal, for his guidance, support and patience on my work. His breadth of knowledge and enthusiasm into problems have always impressed me and inspired my research. The project Professor Lal chose for me well fits my physics background, while drives me to learn more. I am very grateful for the guidance, freedom and financial support he has provided.

I would like to thank my committee member, Professor Lena Kourkoutis. Professor Kourkoutis has always been available to help me in both an academic and a personal level. I also thank Professor David Muller and Professor Joel Brock for their guidance in the master program.

I acknowledge all the professors who have taught me with great energy. I have become a better person because of the wisdom I have gained in the classroom. I also thank the staff for their support - I thank Cynthia Reynolds, Renee King and Sue Bulkley for their help and patience.

I would also like to thank every member in SonicMEMS Lab. A special thank to Mamdouh Abdelmejeed for the technical support and insightful discussions. I thank Justin Kuo and Visarute (Earth) Pinrod, for their guidance in the specimen preparation and experiments setup. As well as Ved Gund, Sachin Nadig, Adarsh Ravi, Alexander Ruyack, Yutong Liu, Leanna Pancoast, Priya Balasubramanian, Benyamin Davaji, Vinaya Kumar, Jiahao Zhang and Nabil Shalabi for friendship and support.

Last, but by no means least, I express my thanks to my beloved parents, for their unwavering love, support and encouragement on my research. I would also like to acknowledge my extended family for their understanding, company and support.

TABLE OF CONTENTS

LIST OF TABLES

LIST OF FIGURES

CHAPTER 1

INTRODUCTION

Scanning Electron Acoustic Microscopy (SEAM) is a technique developed on the basis of a scanning electron microscope (SEM). In SEAM an electron beam (e-beam) with the beam current impacting a target site is modulated at acoustic or ultrasonic frequencies. The absorbed energy of the electrons results in time-varying thermal expansion that leads to acoustic and ultrasonic waves to be launched into the substrate. The waves are detected using a piezoelectric transducer [1, 2]. SEM imaging occurs by the measurement of the bi-products of the tightly focused electron beam and the specimen surface. The bi-products include backscattered electrons, secondary electrons, Auger electrons, X-rays, and photons of various energies. The bi-products are collected on detectors as the e-beam is scanned over the specimen surface. SEM is regularly used to image and analyze the micro- or nano- features of the specimen [3]. In SEAM, the interaction product is an acoustic wave which is detected by a piezoelectric transducer.

SEAM provides unique information in addition to the surface properties provided by SEM. Unlike in SEM, the main contrast of SEAM images is a result of the time-varying thermal gradient induced by the electron energy dissipated in the sample. A SEAM image reveals the thermal and mechanical properties at the site of the e-beam induced heat source. Other mechanisms that lead to mechanical deformation of the specimen can also contribute to the SEAM signals. Contrast from these interactions provide additional electrical properties and magnetic information [4].

SEAM can be readily compared to photo-acoustic imaging (PAI) and Scan-

ning Acoustic Microscopy (SAM). In photo-acoustic imaging (PAI) an acoustically modulated optical beam is absorbed in the sample, inducing an acoustic wave due to the thermal expansion wave. In PAI the optical wavelength is typically in the visible range from 450-800nm, and the resolution is limited by the best optical focus. SEAM has the potential for higher resolution because the spot size of an e-beam can be focused to a much smaller size than a laser beam, down to a few nm.

SEAM is also different from the well-developed scanning acoustic microscope(SAM). Although both SAM and SEAM use acoustic waves as the information carriers and are non-destructive, the contrast mechanisms are different. In SAM, an acoustic wave is generated at GHz frequencies and is focused onto a sample. The reflected and transmitted waves are transduced to image the sample. The resolution of SAM is limited by the ultrasonic wavelength which is on the order of $5 - 10\mu m$ in the GHz frequency range [5]. SAM displays the surface topography and thus surface elastic wave information of specimens while SEAM signals are a function of thermal *and* elastic wave properties [6]. In SEAM, the acoustic wave carries thermal properties of the electron ebam absorption region. Images from SEAM have the resolution determined by the wavelength of the thermal diffusive wave. The experiments in this thesis and past work have shown $\sim \mu m$ resolution with a MHz chopped beam. GHz chopping has the potential for improving the SEAM resolution to the $\sim 100s\ nm$ range, as a much smaller thermal diffusion length determines the resolution.

1.1 Background

SEAM was first developed by Cargill [1] and by Brandis and Rosencwaig [2] independently in 1980s. Since then, a large number of materials including metals [7, 8], semiconductors [9], and ceramics [10] have been imaged and analyzed using SEAM. In these existing examples, the electron beam chopping frequency ranges from 50kHz to a few MHz, and the electron accelerating voltage used is from 10kV to 30kV.

SEAM has shown great potential in obtaining the thermal and elastic properties, subsurface structures, and target electric and magnetic information. SEAM images can be obtained simultaneously with SEM operation. For example, Figure 1.1 compares images obtained from SEAM and SEM, showing that SEAM provides more information on grain boundaries and crystal orientations [11]. Contrast shown in SEAM are due to varying elastic coefficients and acoustic absorption at different orientations. Figure 1.2 displays doping pattern on a GaAs wafer, which illustrates the SEAM sensitivity to local thermal diffusivity coefficients modified by doping [12].

Though SEAM has been proved to succeed in imaging a variety of materials and provides more information than other methods, modeling of the results obtained to the actual material properties is a difficult problem for both analysis and experiments. There are limited theoretical analyses of three dimensions stress field in plate samples. The contrast mechanisms, for example, the magnetic coupling, phase shift due to electron deposition, are still not fully understood. Higher resolution imaging is expected from analysis, but then the achieved resolution is typically worse in practice [13]. A more elaborate trans-

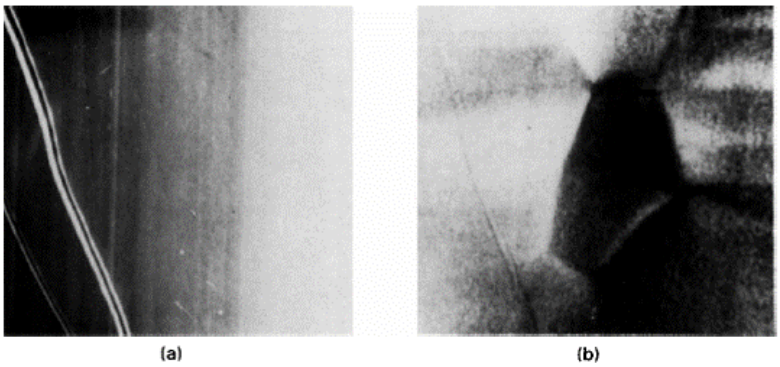

Figure 1.1: SEM(a) and SEAM(b) images of a polycrystalline copper. SEAM shows brightness contrast at the boundaries, causing by the elastic anisotropy.

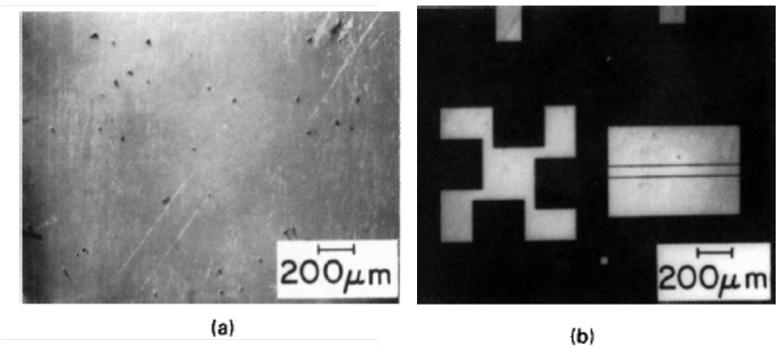

Figure 1.2: SEM(a) and SEAM(b) images of a proton-bombarded GaAs wafer. SEAM is able to image the doping pattern. The dark section was proton bombarded, which modies the thermal diffusivity.

ducer system is needed to operate with high frequency sound waves to achieve higher resolution. E-beam with lower energy might be needed for fragile specimen imaging. A representative application areas of SEAM involve characterization of microelectronics, MEMS structures, individual biological cells, and tissues in 3D.

1.2 Motivation and Approach

We attempt to enhance SEAM imaging to the nanometer range. A GHz chopped e-beam will be used with a GHz resonant aluminum-nitride transducer array system. The modulated e-beam generates a heat source $\sim 10s$ nm in diameter, which determines the spatial resolution of the surface and near surface layers. The propagating acoustic wave has a wavelength of $\sim 5\mu m$, and is picked up by a GHz resonant transducer array. Image processing of pulse data from a large GHz sonic array enables submicrometer range resolution imaging of layers near or below the surface. The effective focus of the transducer phased array can be focused to acquire signals from a specific target surface to enhance resolution and increase the SNR of sonic wavefront imaging.

With unique imaging mechanisms, SEAM will be promising in applications such as nanoscale nondestructive subsurface structure imaging and biomechanical cell imaging at a high speed corresponding to SEM scanning pace. In particular, it is a challenge to understand the role of mechanical properties that effect biological function of cells and the internal building blocks of cells. For example, cell stiffness can be indicative of early signs of eventual transition to a cancerous cell. Being able to quantify cell wall stiffness and adhesion to other cells and surfaces also can serve as indicators of abnormal cell development, which can be controlled by external biochemical signals. Within the cell, the ability to image the stiffness of the mitochondria, the nucleus, endoplasmic reticulum, ribosomes, etc, might lead to an understanding of how modifications of genetic code can modify the mechanical properties and how the mechanical properties can effect cell function. However, at present there is no way to apply probe forces on the nanoscale components within live cells. With SEAM it is possible

to apply forces with a SEM that can be focused to a few nm. However, the consequence of this will be the addition of charge into the cells that would potentially effect cell function. Nevertheless, it seems plausible to explore the possibility of investigating the potential of applying mechanical probes at the nanoscale to insides of cells.

1.2.1 Nanoscale Elasticity and Thermal Properties Imaging

Different from SEM, whose contrast is mainly from different chemical compositions and surface topography, SEAM uses heat generated acoustic waves for imaging. Amplitude of the acoustic waves is determined by the thermal and elastic coefficients. This feature is used to study the mechanical properties of the target specimen. Some applications of SEAM include the characterization of grain structures of 2D materials such as graphene, microelectronic structures, doping profiles, plastic deformation of crystalline metals, are discussed here:

- Grain Structure: In SEAM images, grains with different orientations have brightness contrasts, even in a single phase crystal. The contrast comes from the differences in elasticity. For boundaries of different materials, the contrast might be attributed to different thermal properties in addition to their elastic properties. SEAM could be used to study sub-surface grains that cannot be shown in a SEM alone.
- Charging and dopant properties: SEAM images have been proven to show dopant patterns. The contrast arises from the changes in thermal properties caused by dopant atoms. This advantage combined with the non-destructive subsurface imaging ability makes SEAM a powerful tool in

semiconductor imaging and microelectronics diagnosis [12], where doping variations effect device performance across a wafer.

- Lattice disruptions: For a highly ordered lattice, the fluctuation of acoustic signals is not detectable. However, thermal features (density, specific heat, and especially thermal diffusivity) change significantly with small adjustments, for example, the implantation of foreign ions or mechanical defects. Apart from cracks or delaminations that can be detected by SAM, small crystal defects are expected to be imaged by SEAM [12].

1.2.2 Bio-mechanical Cells Imaging

Biomechanical properties of cells and sub-cellular components play an important role in understanding cell functions and human diseases. Mechanical stress on cells has been proved to affect signal transduction [14], gene expressions [15] and protein production [16]. This area of research focused on mechanobiology is expected to yield new insights in the future [17, 18].

Some of the representative techniques for measuring the mechanical properties of individual cells and molecules include: Atomic Force Microscopy(AFM) maps the topography of cells and local stiffness of the cells surface. The elastic constant is frequency dependent and its measurement is restricted to DC – $100s$ Hz in AFM. AFM provides a lateral resolution of 100nm but sacrifices the imaging speed [19, 20]. Also, the probe tip needs to tap or drag along the cell, which applies a large lateral force on the cell and can possibly deform or damage the specimen. Optical trapping (optical tweezer) can also be used to determine the local stiffness. A bead is controlled by optical radiation forces and applies

forces in the range of 1 to 200 pN on cells. The applied force has an oscillation frequency ranges from 0.1 to 6000Hz [21]. Optical tweezers can transform cells with nanometer precision and obtain sub-micrometer resolution. Shortcomings of optical tweezer are the temperature rise ($\sim 10^{\circ}C$) due to the laser power (250 - 500 mW). It also cannot be used in measuring fast dynamic cellular process ($\sim s$). Magnetic bead microrheometry is used in studying cells viscoelasticity. The bead can produce 100 - 10,000 pN forces and $\sim \mu m$ displacement [22]. The final method – micropipette aspiration, one of the oldest techniques for bio-mechanical measurements, is still a powerful tool in studying cellular deformation. Force ranging from 0.01 - 1000 nN can be applied by micropipette aspiration [23, 24].

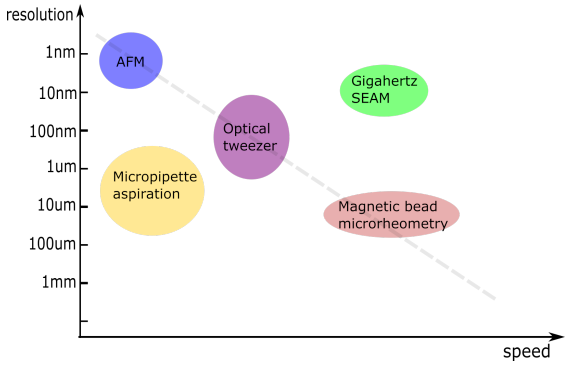

Figure 1.3: The comparison of resolution versus imaging speed of biomechanics measurements techniques.

The various developed techniques have either low resolution or low imaging speed (Figure 1.3). We attempt to develop SEAM to image the biomechanical properties very fast with relatively high resolution. The SEAM approach will not need a bead or a particle label. It will be operated from kHz to GHz, which will reveal the stiffness reaction at high frequency. Cells will be placed in a buffer solution in a microfluidic device. The microfluidic device is covered with

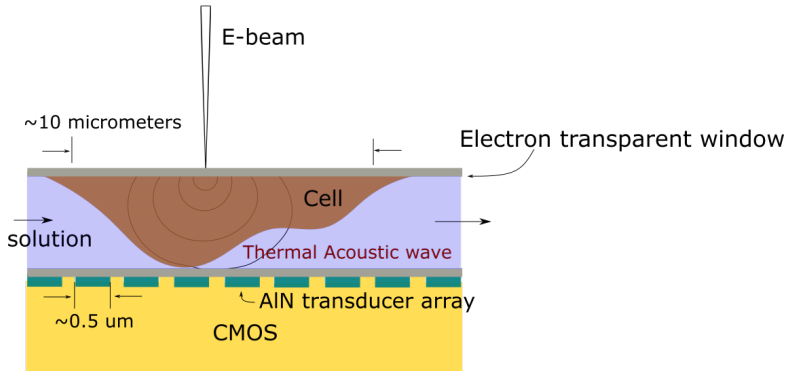

Figure 1.4: Concept of imaging a single cell by gigahertz SEAM.

electron transparent silicon nitride windows [25]. An electron beam with power from 1mW to 100mW, corresponding to 1pJ to 10nJ of energy per period, will be deposited on the cells. The e-beam will generate a 0.01 - 10 Pascal stress in the cell tissue. The microfluidic device is desired to be ultra thin so that the liquid will not attenuate the signal significantly. The AlN transducers need to be placed close to the sample area.

The goal of the work presented in this thesis is to take advantage of the thermal and elastic properties and realizing higher resolution SEAM. The basic phenomena and the generation of thermal acoustic wave will be discussed in Chapter 2. The detection of the acoustic wave using piezoelectric transducers will be covered in Chapter 3. Experimental details and the results will be described in Chapter 4. A summary is given in Chapter 5, together with possible pathways for improved results as future work.

CHAPTER 2

ELECTRON BEAM GENERATED ACOUSTIC WAVE

The structure and operating principle of SEAM are illustrated in Figure 2.1. SEAM is developed on the basis of a commercial scanning electron microscope (SEM), which provides the electron source, focusing lens, scanning coils, specimen stage and vacuum chamber. A pair of electrostatic parallel plates is added to realize beam intensity modulations. A piezoelectric transducer array is attached to the rear side of the specimen for signal detection.

A chopped beam of electrons, serving as a local probe, is incident onto the specimen. The periodically deposited e-beam can be assumed to be a heat flux, which induces thermal expansion and compression. This thermal fluctuation produces an acoustic wave with frequency strongly corresponding to the chopping frequency (normally identical). The amplitude of thermal wave decays to negligible within 1-2 wavelengths, but the acoustic wave it generates can propagate through the substrate. Depending on the pixels location, the acoustic wave propagates through different paths to the detectors, resulting in various amplitudes, time and phase signals at the transducer pixels. Further image processing will allow nondestructive and quantitative evaluation of mechanical properties of the specimen.

This chapter will explore the signal generation source, the heat induced acoustic wave, and the acoustic wave propagation in SEAM.

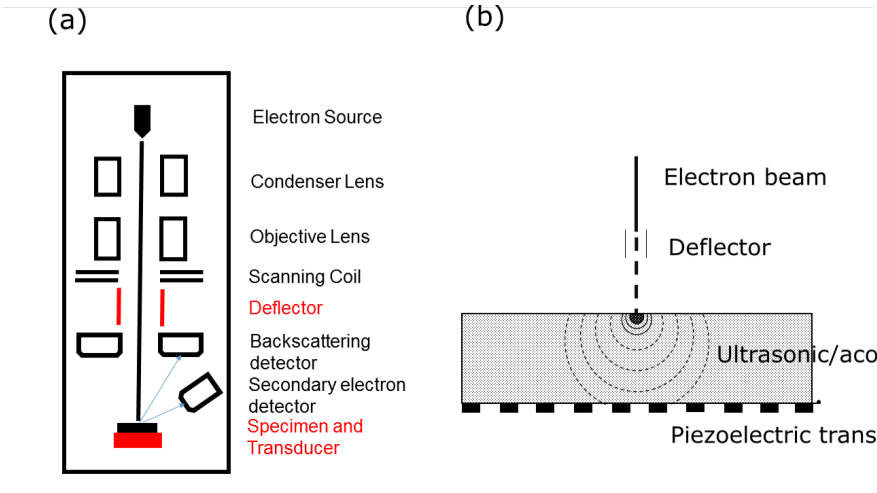

Figure 2.1: (a) SEAM setup. The red parts label a pair of added electrodes and a piezoelectric transducer mounted at the back side of the specimen. (b) SEAM operating principle. The periodically deposited e-beam induces thermal waves and acoustic waves (Filled spot - interaction region, solid line - thermal wave, dash line - acoustic wave).

2.1 Electron Absorption Generated Thermal Flux

When a focused electron beam is incident onto the specimen, a rich variety of interactions are involved. The interaction volume determines the source size of signals, which limits to the spatial resolution of SEAM. Therefore, it is important to study how interactions happen between electrons and the specimen, and what influence they have on the SEAM signals.

2.1.1 Electron-Specimen Interaction

The electron-specimen interactions are classified into elastic scattering events and inelastic scattering events. Elastic scattering events change the direction of propagation, while the kinetic energy of the incident electron remains con-

served. Inelastic scattering events result in the energy transfer between incident electrons and electron shells of the target atoms, accompanied by various forms of energy loss [3]. Eventually, a significant portion of the total kinetic energy of incident electrons is transformed into heat , which is the source of the elastic wave. Most of the heat is generated within the interaction volume. A quantitative study of the interaction size is needed to estimate the resolution obtainable in SEAM.

Although the diameter of an electron beam probe can be narrowed down to a few nanometers, the interaction range is determined by the scattering processes. Both elastic scattering and inelastic scattering interactions contribute to the final electron distribution profile. Bethe range estimates the traveling range by integrating the average energy loss over the total electron kinetic energy. However, it overestimates the interaction volume because the deviation in electron direction caused by elastic interactions is not taken into consideration. A more appropriate expression of the interaction volume is the Kanaya-Okayama Range (KO range). KO range considers the combined effects of all scattering events. It treats the interaction volume as a hemisphere and gives the expression for interaction radius (in μm):

$$R_{KO} = \frac{0.0276 A E_0^{1.67}}{Z^{0.89} \rho} \tag{2.1}$$

where E_0 is the incident electron energy in keV, A is the target atomic weight in $g/mole$, ρ is the target density in g/cm^3, and Z is the target atomic number.

An exact expression for electron probe depth is hard to obtain mathematically. The Bethe range and KO range only take into account a limited number of influencing factors. Besides, the energy deposition is nonuniform inside the volume. A numerical Monte Carlo simulation, instead, illustrates the in-

teraction volume more precisely by incorporating a wide range of effects numerically. Good quantitative agreement has been found between the calculated energy dissipation profile and the experimental etching profile for polymethylmethacrylate (PMMA) (shown in Figure 2.2) [26].

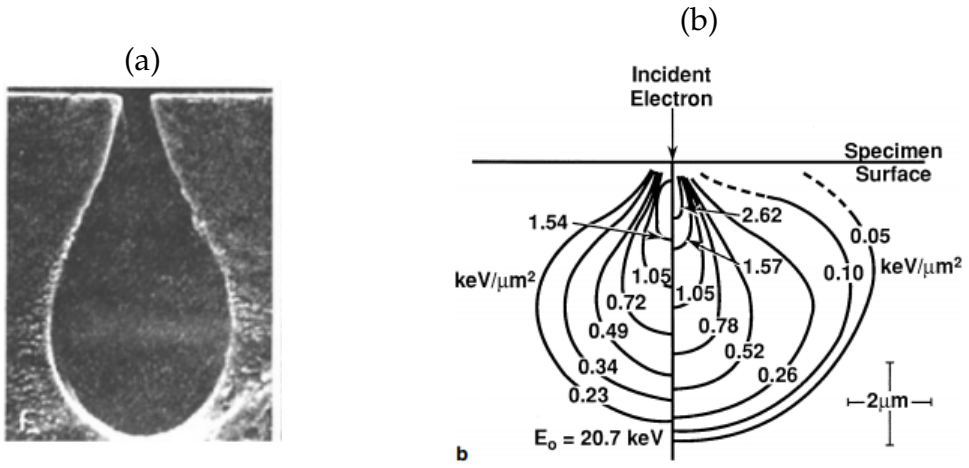

Figure 2.2: (a) Etching profile of PMMA. (b) Comparision of experimental data(left) with Monte Carlo calculation(right).

As the term "Monte Carlo" suggests, the single trajectory of an electron is generated randomly and cannot be replicated. However, simulations of over 10^4 electrons would provide a statistical interaction volume shape. Figure 2.3 shows the simulated volumes for incident electrons with different energies. At low energy (≤1keV), the diameter of the focused e-beam spot affects the interaction volume significantly. As energy increases, the impact of the e-beam size becomes negligible compared to the strong scattering events.

The size of the interaction volume largely depends on the energy of the primary e-beam (Figure 2.3, simulated with reference [27]). This can be understood from the cross section $Q \sim 1/E^2$. Moreover, the travel distance for a single step is estimated by the energy loss $dE/ds \sim 1/E$ (Bethe range [3]). As the e-beam energy increases, an electrons penetrates deeper before being scattered and travels

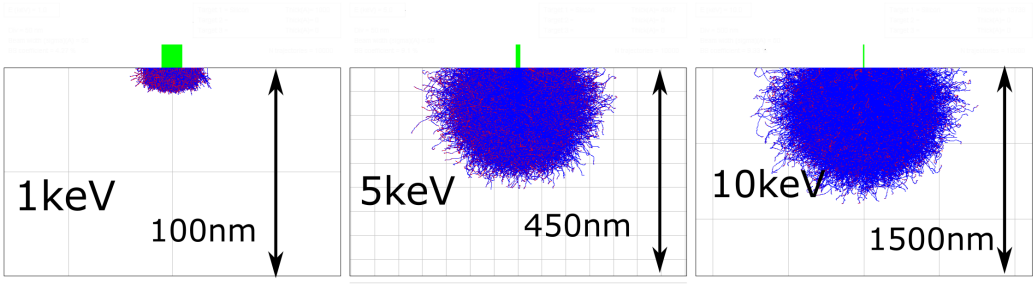

Figure 2.3: Monte Carlo simulation of interaction profile.The target material is silicon. 10^4 electrons trajectories are plotted; beam width used is 5*nm* for all cases.

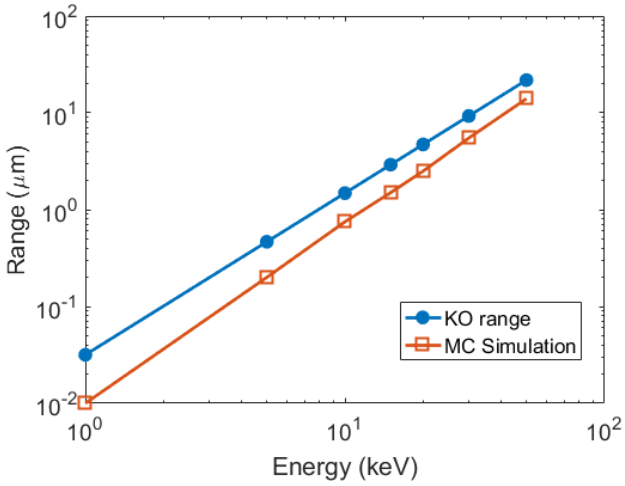

Figure 2.4: Comparison between KO range and Monte Carlo Simulation range. The material used is Silicon.

further until the total energy falls below to the cutoff range, which causes the "tear drop" absorption pattern (Figure 2.2).

Figure 2.4 compares the interaction range from the KO prediction and the Monte Carlo simulation. Results from these two approaches are of the same order of magnitude. As energy increases, the mathematical calculation and the numerical simulation match more closely.

2.1.2 SEAM Resolution

The resolution of SEAM strongly depends on the heat generation region. The heated area can be treated as a function of e-beam diameter d_B, interaction depth d_s and thermal diffusion length d_T. The e-beam diameter is determined by the focusing lens of the SEM. The state-of-the-art SEM beam probe can be focused down to a few nanometers [3]. However, the interaction depth and thermal diffusion length can be much larger than the beam spot size (Table 2.1). The interaction depth can be treated as the radius of the interaction volume discussed in Section **2.1.1**. The thermal diffusion length represents the distance that a thermal wave can travel before decaying down to 1/e of the original amplitude. It can be expressed as

$$d_T^2 = \frac{2\kappa}{\omega} = \frac{2K}{\omega\rho C} \tag{2.2}$$

where κ is the thermal diffusivity in m^2/s , ω is the heating angular frequency in Hz, K is the thermal conductivity in $W/m^\circ C$, ρ is density in kg/m^3 and C is the specific heat in $J/kg^\circ C$. Thermal diffusion length is a representation of the thermal properties of the target material, as a function of the chopping frequency of the electron beam. For example, thermal conductivity itself can be a function of frequency [28, 29].

Considering all these impact factors, Cargill defined a total effective source diameter to describe the resolution of the SEAM [1]:

$$D = (d_B^2 + d_S^2 + d_T^2)^{1/2} \tag{2.3}$$

As can be seen from Eq. 2.3, the e-beam size and energy, the chopping frequency, and the thermal property all contribute to the resolution of SEAM. The decrease of the effective source diameter D leads to better spatial resolution. Therefore, it

Table 2.1: Acoustic wave source parameters with a 5MHz(up) and a 1.3GHz(down) chopped e-beam. Assume the beam size is d_B = 50nm. d_s is calculated by KO range.

5MHz chopped beam with energy E = 30keV

	Au	Cu	Al	Si	water
d_s (μm)	1.69	2.88	8.22	8.31	18.75
d_T (μm)	2.84	2.66	2.49	2.37	0.095
D (μm)	3.31	3.92	8.58	8.64	18.75

1.3GHz chopped beam with energy E = 10keV

	Au	Cu	Al	Si	water
d_s (μm)	0.27	0.46	1.31	1.33	2.99
d_T (μm)	0.18	0.16	0.15	0.15	0.0059
D (μm)	0.32	0.49	1.32	1.34	2.99

is desired to use a higher chopping frequency for the shorter thermal depth and a lower energy for the smaller interaction volume.

Values of effective source diameter D for several materials are shown in Table 2.1. Thermal parameters were used from reference [30, 31]. As can be seen, thermal coefficients significantly influence the thermal diffusion length d_T. For high thermal expansion material such as metals, d_T dominates the resolution of SEAM imaging. Moreover, concerning the 30keV e-beam chopped at MHz, thermal diffusion and electrons scattering have almost the same impacts on the size of the heat source. At 1.3GHz chopping frequency, the thermal diffusion length is $\sim 10 - 100nm$. A few hundred nanometers range interaction depth d_s can be obtained with 10keV e-beam energy. The effective source diameter D is controlled within a few hundreds nanometer, and leads to sub-micrometer resolution with GHz-SEAM (Table 2.1).

The previous SEAM images were obtained with chopping frequencies from kHz to a few MHz and with e-beam energies from 10 to 30keV. Here, We investigate the performance of SEAM with e-beam being chopped at 1-2 GHz and e-beam energy at 1-10keV. A GHz chopped e-beam produces a shorter wavelength acoustic wave with better diffraction performances, and a smaller heat generation volume. These factors are promising in pushing acoustic imaging to the nanometer range.

2.1.3 Three Dimensional Imaging

SEAM is also promising in getting three dimensional structures of layers underneath the surface. This can be performed by varying the e-beam energy in order to generate heat at different depths. The electron-specimen interaction profile has a teardrop shape for high energy beam (Figure 2.2), and consequently most of the heat is dissipated underneath the surface. The detected acoustic wave carries the thermal information and the elastic properties of the heat source and only the elastic information of the propagating medium. A 3D image of the layers can be constructed from further image processing

2.2 Thermal Acoustic Wave Generation

Four mechanisms have been proposed to explain the acoustic wave generation due to incident electrons: (1) the thermal gradient, (2) excess carriers, (3) piezoelectric coupling, and (4) electrostrictive and magnetostrictive coupling. The heat induced acoustic wave mechanism has been discussed by many authors

in detail and plays a dominant role for most of the materials [32]. The latter three mechanisms have been demonstrated in experiments, but theory has not been developed in detail. The excess carrier mechanism [33] yields a reasonable explanation for contrasts shown in metal and semiconductor cases. Some ceramic materials might need to be analyzed with the piezoelectric effect [34, 10]. Ferromagnetic materials showed contrast suggesting magnetic coupling but the result cannot be explained yet. We limit the scope of this thesis to the heat induced acoustic wave.

When a time-varying e-beam is focused on the specimen surface, the thermal fluctuations would produce a thermal wave and consequently an acoustic waves. The thermal wave is a diffusive wave and decays to a negligible amplitude after traveling 1-2 wavelength ($\lambda_{thermal} = 2\pi d_T$) . However, the acoustic wave generated by this thermal variation carries the thermal characteristics of the SEAM source. The acoustic wave travels through the specimen and is detected by the piezoelectric transducers at the rear side. To characterize the target specimen, we have to relate the detected acoustic wave with the input heating source.

2.2.1 Thermal Diffusion Equation

The thermal diffusion equation will be used to determine the local temperature change due to incident electrons. Several assumptions are made on the periodically deposited e-beam:

1. The e-beam is treated as a uniformly distributed spot source. (The actual electron beam obeys the Gaussian distribution and shows blur at the edge

[35, 36].)

2. The absorbed energy is considered to be the kinetic energy of all incident electrons except the backscattered portion.
3. All absorbed electron kinetic energy is transformed to heat.
4. The absorption of energy happens at the surface of the specimen.

The problem may be treated more accurately, but with greater difficulties, if the exact amount of absorbed energy and heat distribution are taken into consideration.

An e-beam of current (I) is accelerated by voltages (V). We neglect the energy lost by all other forms except backscattered electrons (assumption 2). This can be compensated to some extent by the overestimation of energy carried by the backscattered electrons. The portion of backscattered electrons can be estimated by [37]

$$\eta_{BS} = E^m C \tag{2.4}$$

where $m = 0.1382 - \frac{0.9211}{Z^{1/2}}$, and $C = 0.1904 - 0.2235(lnZ) + 0.1292(lnZ)^2 - 0.01491(lnZ)^3$. The power absorbed by the specimen is

$$P = (1 - \eta_{BS})IV = \eta IV \tag{2.5}$$

where η is the absorbed electrons percentage. Considering assumption 1, the deposited heat power density can be expressed as the absorbed power divided by the e-beam size (A_{ebeam}). After being chopped, the electron beam serves as a harmonically varying heat flux

$$p = \frac{\eta\, I\, V}{A_{ebeam}} \exp(j\omega t) \tag{2.6}$$

For e-beam modulated by a square wave, the deposited power density can be expressed as

$$p_{square} = \frac{\eta\, I\, V}{A_{ebeam}} \sum_{i=1}^{n} \exp(jn\omega_0 t) \tag{2.7}$$

where ω_0 is 2π times the chopping frequency. The high harmonic components go beyond the bandwidth of the transducers, thus we can focus on the primary frequency f_0.

The temperature distribution can be obtained from the heat diffusion equation with a heat source at the boundary:

$$\begin{aligned} &\textit{Governing Equation}: && K\,\nabla^2\Theta = \rho\, C\, \frac{\partial\Theta}{\partial t} \\ &\textit{Boundary Condition}: && \frac{\partial\Theta}{\partial t}|_{surface} = \frac{1}{\rho C} p \end{aligned} \tag{2.8}$$

The temperature is determined by time and position independently. Considering a one-dimensional problem in the incident direction, the temperature can be expressed as $\Theta(x,t) = f(x)g(t)$. The partial differential equation Eq. 2.8 can then be converted into two ordinary differential equations. The ODEs can be solved using the Wronskian, Frobenius or integrating factors method. The solution is

$$\Theta = \frac{\eta\, I\, V}{A_{ebeam}} \left(\frac{\kappa}{\omega}\right)^{1/2} K^{-1}\, e^{j(\omega t)}\, e^{-x\,(\frac{\omega}{2\kappa})^{1/2}\,(1+j)} \tag{2.9}$$

Note that the temperature mentioned represents the temperature changes above the nominal temperature due to the electron bombardment.

Figure 2.5 displays the temperature distribution and thermal gradient distribution with respect to the penetration depth. The local temperature decays to zero within $1\mu m$ range, which agrees with the thermal depth range discussed in section 2.1.2. The thermal depth is defined as the propagation distance where the amplitude of the thermal wave decays by a factor of 1/e. The mathematical expression of d_T comes from Eq. 2.8.

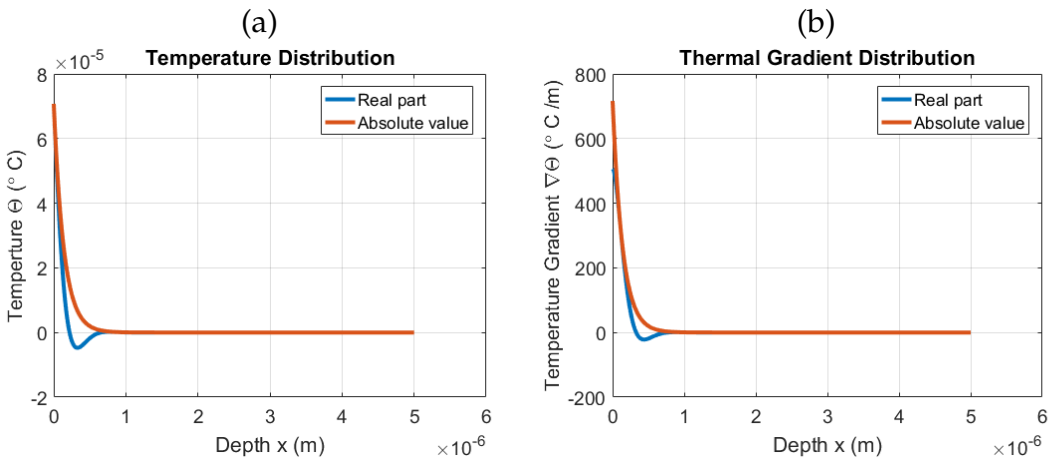

Figure 2.5: Temperature distribution (a) and temperature gradient distribution (b) along the incident x direction. (Calculated for a chopped e-beam at 1.3GHz with power density 10^5 W/m^2 shot on silicon.)

Figure 2.6 demonstrates the absolute value of the temperature gradient as a function of the chopping frequency and the penetration depth. The temperature gradient decays quickly as the depth and the frequency increase. Therefore, higher chopping frequency results in better resolution.

2.2.2 Acoustic Wave Equation with Heating Source

Having obtained the temperature distribution, we need to relate the local displacement with the temperature change. The equation of motion illustrates how thermal energy transforms to the mechanical domains and how the thermal acoustic wave is generated.

The bombardment of electrons at the specimen surface causes a non-uniform temperature distribution, which results in a thermally generated strain

$$S_\Theta = \alpha\Theta \tag{2.10}$$

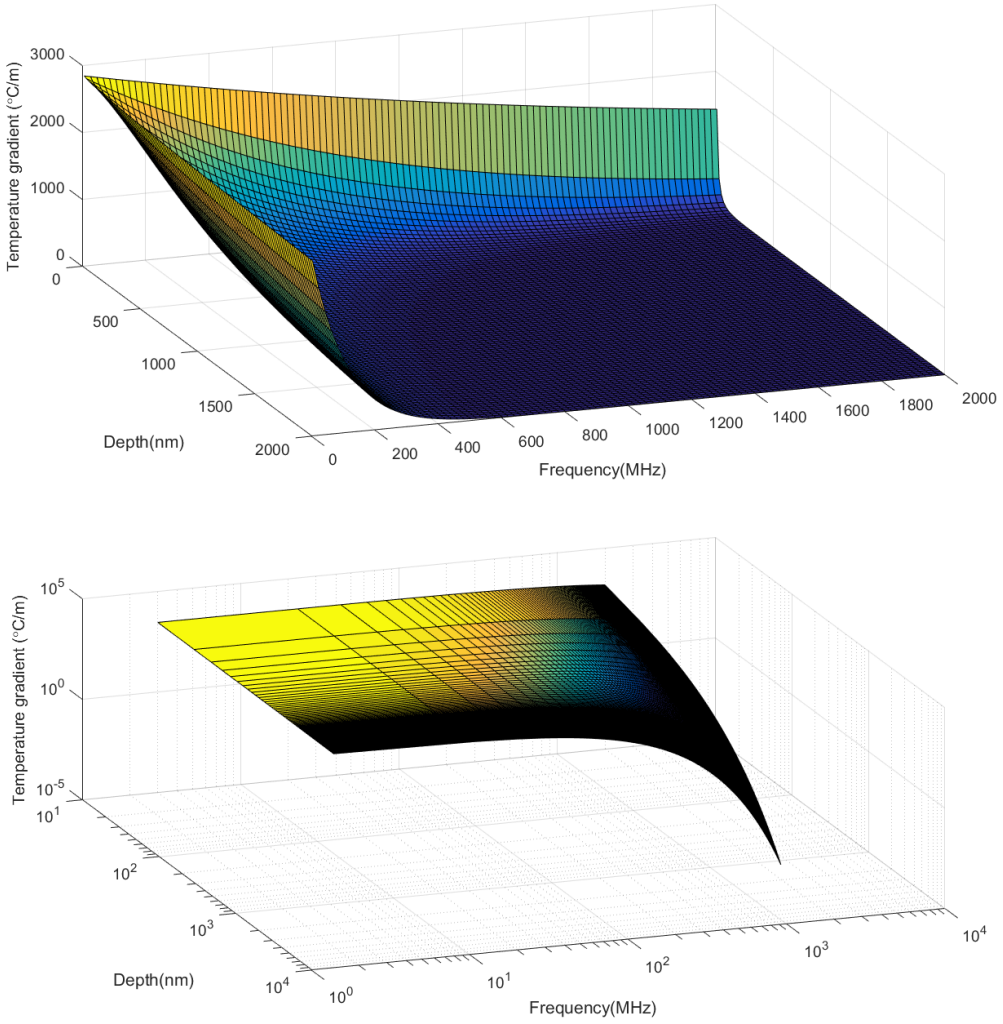

Figure 2.6: Temperature gradient variation with respect to penetration depth and chopping frequency. TOP: linear scale. BOTTOM: Log scale.

where α is the thermal expansion coefficient. The mechanical stress T can also produce deformation and mechanical strain S_m. Their relation is described by the constitutive equation

$$T = cS_m \tag{2.11}$$

where c is the stiffness elements of the matrix being considered (units N/m^2).

The total strain is a combination of both effects

$$S = \frac{\partial u_i}{\partial x_j} = S_\Theta + S_m \tag{2.12}$$

which could be written as

$$T = cS - \alpha c\Theta \tag{2.13}$$

Obeying Newton second law F = ma , the stress are related with displacement by [38]

$$\rho \frac{\partial^2 u}{\partial t^2} = \nabla \cdot T \tag{2.14}$$

Substitution of Eq. 2.13 in Eq. 2.14 results in the equation of motion

$$\rho \frac{\partial^2 u}{\partial t^2} = \nabla \cdot (c\nabla u - \alpha c\Theta) \tag{2.15}$$

As can be seen from Eq. 2.15, the thermal gradient serves as the driving force for particle displacement. The thermal gradient is highly dependent on chopping frequency (Figure 2.6) . As frequency increases, $\partial\Theta/\partial x$ decays in the form $\sim \frac{1}{\omega^{1/2}} e^{-x(\omega/2\kappa)^{1/2}}$. Also, two materials with large differences in thermal expansion coefficient α, density ρ and Young's modulus c would result in great contrast in SEAM.

Considering the case of a traveling elastic wave in an isotropic medium, the equation of motion can be simplified to

$$\rho \frac{\partial^2 u}{\partial t^2} = (\lambda + 2\mu)\nabla(\nabla \cdot u) - \mu\nabla \times \nabla \times u - \alpha(3\lambda + 2\mu)\nabla\Theta \tag{2.16}$$

where λ and μ are the Lame constants representing the modulus of elasticity. The elastic displacement vector $\boldsymbol{u}$ can be written as a linear combination of the gradient of a scalar and the curl of a vector quantities as

$$\boldsymbol{u} = \nabla\phi + \nabla \times \boldsymbol{\psi} \tag{2.17}$$

Therefore, we have

$$\nabla \cdot \boldsymbol{u} = \nabla \cdot (\nabla\phi + \nabla \times \boldsymbol{\psi}) = \nabla^2\phi$$
$$\nabla \times \boldsymbol{u} = \nabla \times (\nabla\phi + \nabla \times \boldsymbol{\psi}) = \nabla \times \nabla \times \boldsymbol{\psi} \tag{2.18}$$

5Apply the $\nabla \cdot$ operator to Eq. 2.16 to obtain

$$\rho\frac{\partial^2}{\partial t^2}\nabla \cdot \boldsymbol{u} = (\lambda + 2\mu)\nabla \cdot \nabla(\nabla \cdot \boldsymbol{u}) - \mu\nabla \cdot (\nabla \times \nabla \times \boldsymbol{u}) - \alpha(3\lambda + 2\mu)\nabla^2\Theta \tag{2.19a}$$

Substitute the displacement $\boldsymbol{u}$ with Eq. 2.17 and use the identity $\nabla \cdot (\nabla \times \boldsymbol{\psi}) = 0$ to get

$$\rho\frac{\partial^2}{\partial t^2}\phi = (\lambda + 2\mu)\nabla^2\phi - \alpha(3\lambda + 2\mu)\Theta \tag{2.19b}$$

This is the governing equation for the longitudinal wave traveling in an isotropic medium. For a harmonic heat source, the wave number and propagating speed are

$$k_l = \frac{\omega^2\rho}{\lambda + 2\mu} = \frac{\omega^2}{v_l^2} \tag{2.20}$$

$$v_l = \sqrt{\frac{c}{\rho}} = \sqrt{\frac{\lambda + 2\mu}{\rho}} \tag{2.21}$$

where ω is the angular frequency.

Apply the $\nabla\times$ operator to Eq. 2.16 to obtain:

$$\rho\frac{\partial^2}{\partial t^2}\nabla \times \boldsymbol{u} = (\lambda + 2\mu)\nabla \times \nabla(\nabla \cdot \boldsymbol{u}) - \mu\nabla \times (\nabla \times \nabla \times \boldsymbol{u}) - \alpha(3\lambda + 2\mu)\nabla^2\Theta \tag{2.22a}$$

and use the identity $\nabla \times (\nabla\phi) = 0$, one can get

$$\rho\frac{\partial^2}{\partial t^2}\boldsymbol{\psi} = \mu\nabla^2\boldsymbol{\psi} \tag{2.22b}$$

which is the governing equation for the shear wave. Shear wave factor and wave velocity can be obtained in the same way as done for longitudinal waves.

Figure 2.7 illustrates the behavior of a longitudinal wave and a shear wave. The particle in a longitudinal wave moves along the propagating direction, while in a shear wave the particle oscillates perpendicular to the traveling direction [39]. When the radius of the heat source is much larger the thermal wavelength, the impact of shear waves can be neglected as the heat source is spreading over a region much larger than the thermal diffusion depth [40]. The electron beam we used can only be focused down to ~0.5mm, which is much larger than the thermal wavelength. Therefore, we only consider the displacement caused by longitudinal waves here. All excited waves should be taken into account for a more complete and accurate prediction in SEAM. However, the assumption of only longitudinal waves provides a simplified solution for particle displacement and applied stress, enabling an insight into the signal amplitude.

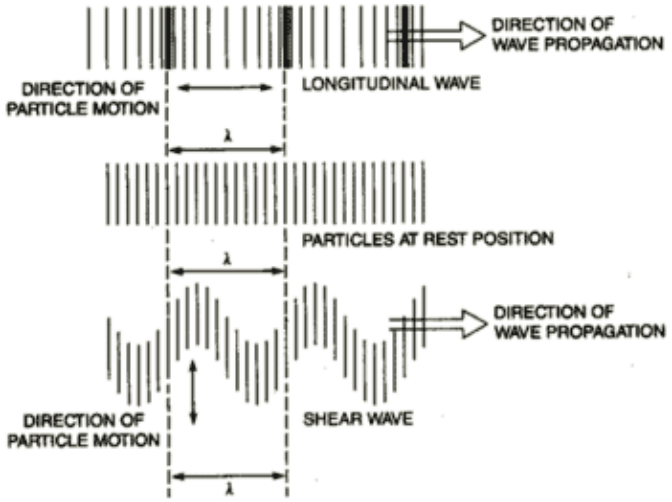

Figure 2.7: Longitudinal wave and Shear wave.

To solve the longitudinal wave equation, Eq. 2.19 can be rewritten as

$$\frac{\partial^2}{\partial x^2}\phi + k_l^2\phi = \frac{\alpha\rho}{v_l^2}\Theta \tag{2.23}$$

The temperature distribution from Eq. 2.9 can be written as [32]

$$\Theta(x) = \Theta_0 e^{-\tau x} \tag{2.24a}$$

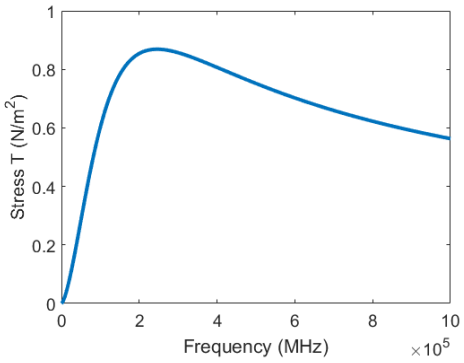

Figure 2.8: The heat induced stress dependence on chopping frequency.

where $\Theta_0 = \Theta(x = 0) = \frac{\eta\ I\ V}{A_{ebeam}}\ (\frac{\kappa}{\omega})^{1/2}\ K^{-1}$ and $\tau = \sqrt{\frac{\omega}{2\kappa}}(1 + j)$. Define β as $\beta = (3\lambda + 2\mu)\alpha/\rho v_L^2$. Eq. 2.23 has the solution:

$$\phi = \alpha\Theta_0 \frac{1}{\tau^2 + k_l^2} e^{-\tau x} + A \frac{-\tau\beta}{\tau^2 + k_l^2} e^{-ik_l x} \tag{2.25}$$

where A is a constant that need to be set by the boundary condition.

Knowing that $u = \partial\phi/\partial x$ and the specimen surface is free $\partial u/\partial x|_{x=0} = -\beta\Theta_0$, the displacement is obtained as

$$u(x) = j\frac{k_l\beta\Theta_0}{k_l^2 + \tau^2} e^{-jk_l x} - \frac{\tau\beta\Theta_0}{k_l^2 + \tau^2} e^{-\tau x} \tag{2.26}$$

The strain and stress are (Eq. 2.12 and Eq. 2.14)

$$S_{xx} = \frac{k_l^2\ \beta\ \Theta_0}{k_l^2 + \tau^2} e^{-jk_l x} + \frac{\tau^2\ \beta\ \Theta_0}{k_l^2 + \tau^2} e^{-\tau x} \tag{2.27}$$

$$T_{xx} = \rho v_l^2 \frac{k_l^2}{k_l^2 + \tau^2} \beta\Theta_0 (e^{-jk_l x} - e^{-\tau x}) \tag{2.28}$$

As can be seen from Figure 2.8, the amplitude of the stress increases to a peak at ~260GHz chopping frequency, and then decreases. For the SEAM operating frequency (kHz-GHz), a higher chopping frequency corresponds to a larger stress where all other parameters including the source generation volume remain constants.

CHAPTER 3

ACOUSTIC WAVE DETECTION

The previous chapter discusses the the particle displacement and the stress due to heat induced acoustic waves. In this chapter, we covers the techniques used to measure those quantities. Piezoelectric transducers are used to transform signals from the mechanical domain to the measurable electrical domain. The current from a transducer can be measured by a trans-impedance amplifier or a lock-in amplifier for high SNR.

3.1 Piezoelectric Materials

3.1.1 Piezoelectric Properties

In most materials, there is no coupling between the electrical and mechanical domains. However, piezoelectric materials show unique properties such that an applied stress changes their electrical polarization and induces electricity. The constituent relations for piezoelectric materials are [41]:

$$T = c^E S - eE, \quad D = eS + \epsilon^T E \tag{3.1a}$$

$$S = \frac{1}{c^E} T + dE, \quad D = dT + \epsilon^T E \tag{3.1b}$$

$$S = \frac{1}{c^D} T + gD, \quad E = -gT + \frac{1}{\epsilon^T} D \tag{3.1c}$$

$$T = c^D S - hD, \quad E = -hS + \frac{1}{\epsilon^S} D \tag{3.1d}$$

Table 3.1: Piezoelectric coefficients

T	Stress vector	N/m^2
S	Stress vector	m/m
E	Electric field vector	V/m
D	vector of electric displacement	C/m^2
ϵ	Permitivity	F/m
c	Matrix of compliance coefficients	m^2/N
d	Matrix of piezoelectric constants (charge)	N/V
g	Matrix of piezoelectric constants (voltage)	m^2/C
e	Matrix of piezoelectric modulus (strain)	C/m^2
h	Matrix of piezoelectric modulus	V/m

The superscript represents the variable that is held constant.Table 3.1 gives the piezoelectric coefficients and their units.

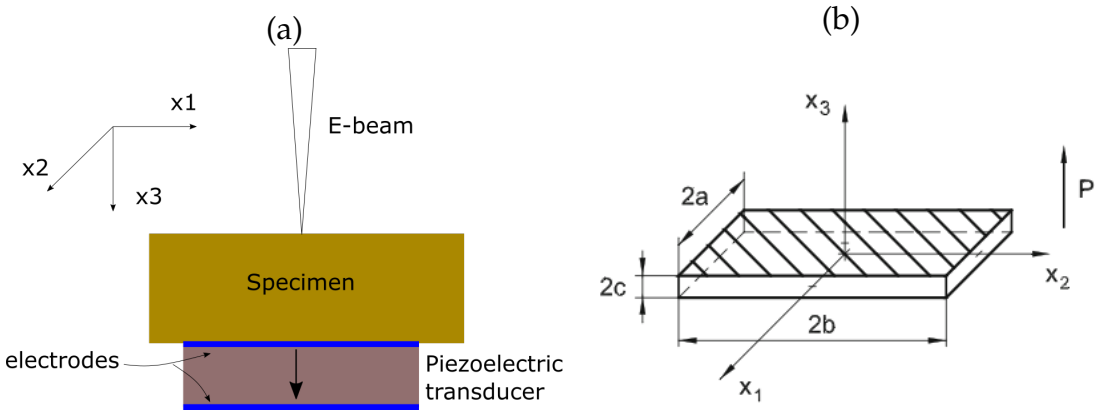

Figure 3.1: (a) Sketch of the specimen assembly. The transducer is attached at the back side of the top specimen (the polarization direction can be up or down). (b) Piezoelectric material in thickness mode. $a \gg c$, $b \gg c$, polarized in the x_3 direction.

Considering the geometric structure of our assembled specimen (Figure 3.1),

the launched acoustic wave induced by the e-beam excites the crystal in its thickness mode. Eq. 3.1b is used in the form

$$D_3 = d_{33}T_3 + \epsilon_{33}^T E_3 \tag{3.2}$$

Electrical signals from the transducers can be measured in voltage or current. For a voltage measurement, the piezoelectric crystal introduces an open terminal circuit. The output voltage is

$$V = \int_{-t/2}^{t/2} E_3 \, dx_3 = \int_{-t/2}^{t/2} (-\frac{d_{33}}{\epsilon_{33}^T} T_3) \, dx_3 = \int_{-t/2}^{t/2} (-g_{33}T_3) \, dx_3 \tag{3.3}$$

where t is the thickness of the transducer. Assuming stress T_3 is uniform across the total thickness t, the voltage is estimated to be

$$V = -g_{33} \, t \, \rho \, v_l^2 \frac{k_l^2}{k_l^2 + \tau^2} \beta\Theta_0 (e^{-jk_l t} - e^{-\tau t}) \tag{3.4}$$

For a current measurement, the short circuit current is

$$I = \frac{d}{dt} \int D_3 \, dA = \frac{d}{dt} \int d_{33}T_3 \, dA = \omega \int d_{33}T_3 \, dA \tag{3.5}$$

where A is the area of a piezoelectric transducer in the x_1 and x_2 directions. Assume the wave distributes uniformly in the $x1$, $x2$ cross section. The current becomes

$$I = \omega \, A \, d_{33} \, \rho \, v_l^2 \frac{k_l^2}{k_l^2 + \tau^2} \beta\Theta_0 (e^{-jk_l t} - e^{-\tau t}) \tag{3.6}$$

The trans-impedance amplifier can be used to change the current to measurable voltage.

3.1.2 Resonances of PZT Transducers

Piezoelectric materials have frequency dependent polarization. Assuming nonlinearity is small, the periodic stress is transformed into the electrical domain

at the same frequency. For a piezoelectric transducer operating in the thickness mode, the electrical impedance is [42]

$$Z = \frac{1}{j\omega C_0}[1 - k_T^2 \frac{tan(\gamma t/2)}{\gamma t/2}] \tag{3.7}$$

where C_0 is the clamped capacitance of the transducer, $k_T = \frac{k_{33}^2}{1+k_{33}^2}$ and $k_{33}^2 = \frac{e_{33}^2}{\epsilon_z^s c_{33}^E}$, $\gamma = \frac{\rho\omega^2}{c_{33}^D}(1 - \frac{\eta j}{\rho\omega})$ and η is the lossy factor. It has the equivalent circuit shown in Figure 3.2 [43]. The impedance frequency dependence is displayed in Figure 3.3 [43]. As frequency increases, a piezoelectric plate approach its resonant frequency f_m first, at which the transform efficiency between the electrical domain and the mechanical domain is the highest. As the frequency keeps increasing, the plate reaches the anti-impedance f_n at which the impedance is a local maximum.

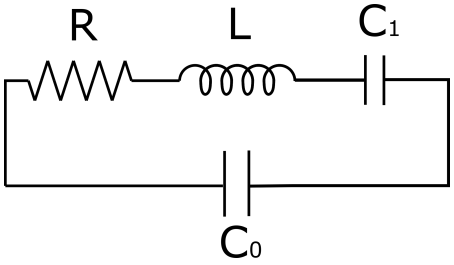

Figure 3.2: Piezoelectric transducer equivalent circuit.

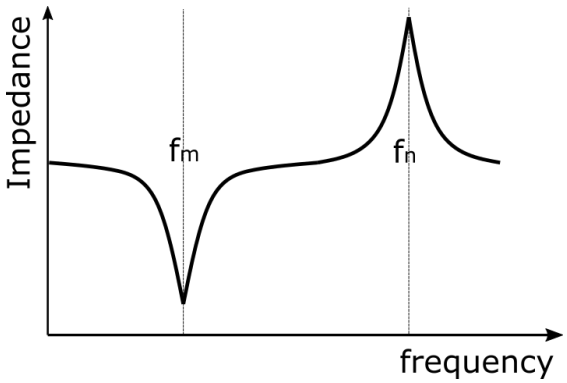

Figure 3.3: Piezoelectric material impedance curve in thickness mode.

The mechanical quality factor Q_m of the material is defined as the energy stored divided by the energy dissipated over one period. For piezoelectric materials, Q_m is [43]

$$Q_m = \frac{f_n^2}{2\pi f_m C_0 Z_m (f_n^2 - f_m^2)} \tag{3.8}$$

where C_0 is the clamped capacitance (Figure 3.2), f_m, f_n are the resonance and

anti-resonance frequencies (Figure 3.3) and Z_m is the impedance at f_m. Higher Q_m results in more energy transferred to the electrical signal, and thus a higher signal to noise ratio measurement at this frequency .

3.2 Piezoelectric Phased Arrays

In previous SEAM work, the detectors used are bulk piezoelectric transducers. We plan to use a phased transducer array to get higher resolution.

The phased array can be used to study anisotropy in wave generation due to electron beam bombardment in the specimen. As the name "phased" suggests, the transducer arrays can tell the time differences among received signals. Based on the wave physics and antenna array theory, a pattern of the source region can be investigated.

3.3 Approaches for High Signal-to-Noise Ratio Detection

In electrical measurements, it is desired to have a large Signal-to-Noise Ratio (SNR). Two approaches can be used in SEAM to improve the SNR.

Trans-Impedance Amplifier(TIA): TIA converts current to voltage (Figure 3.4). It can be used to magnify the current generated by a piezoelectric transducer. Following the op amp golden rules, there is no voltage difference between the positive and negative inputs. The generated current flows through the feedback resistor R_f, and gives an output voltage

$$V_{TIA} = -IR_f \tag{3.9}$$

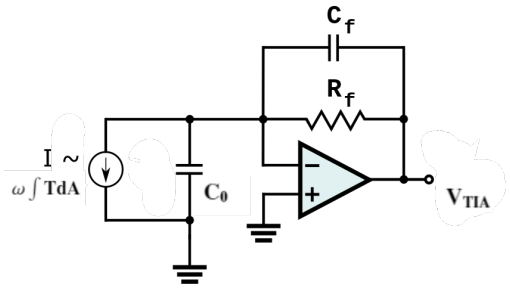

Figure 3.4: Trans-impedance amplifier circuit diagram.

In SEAM, the piezoelectric material can be modeled as a current source owing to the constitutive equation. The transducer is ground connected at one side and is connected to the TIA virtual ground at the other electrode. Stress induced current would be amplified by the feedback resistor with a value of R_f. Combing with Eq. 3.5, the output voltage versus stress input is:

$$V_{TIA} = -\omega \int d_{33} T_3 dA \times R_f \tag{3.10}$$

Lock-in Amplifier: A lock-in amplifier extracts the signal at the desired frequency and rejects noise outside the band frequency range. The lock-in amplifier can narrow the bandwidth and subtract small voltage signals. In SEAM, the chopping frequency is normally set to be the reference frequency, whereas using 2f or 3f might result in novel nonlinear imaging [44].

CHAPTER 4

EXPERIMENTAL RESULTS

4.1 Experiment Apparatus

Equipment setup is shown in Figure 4.1. A Kimball Physics EMG4212 Electron gun was used to generate an e-beam of 10–100μA current. A 1 – 10kV accelerating voltage was employed on electrons emitted from the filament. The spot size of the e-beam was focused to ~0.5mm in diameter. A chopping system and transducer output feedthroughs were added for thermal acoustic signal generation and detection.

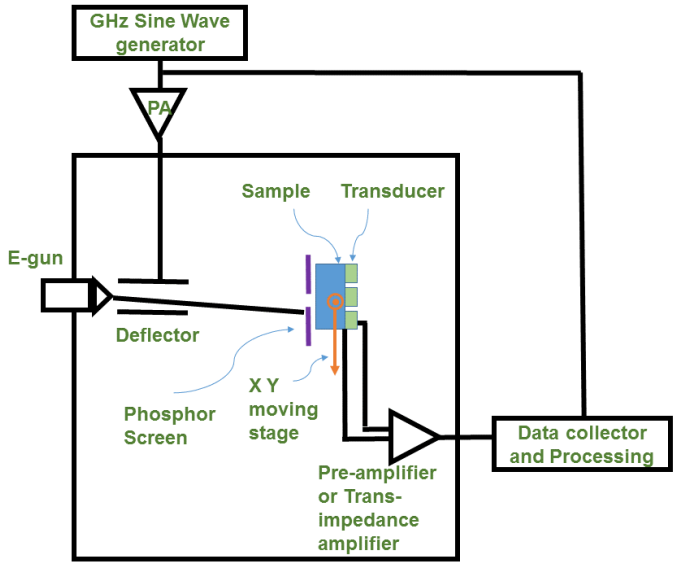

Figure 4.1: Equipment Setup

A deflector was mounted across the e-beam path. A grounded phosphor screen with a hole in its center was placed right in front of the specimen. This phosphor screen is used to locate the e-beam position and to block the electrons.

Only part of the deflected electrons can go straight into the hole and reach the specimen surface. Other electrons are blocked by the phosphor screen. Accordingly, the e-beam energy deposits intermittently on the specimen surface. The output from the transducer was fed to a preamplifier or a TIA. The specimen was fixed on a NewPort AG-LS25-V6 X-Y stage for scanning imaging.

Different deflectors were used for MHz and GHz e-beam blanking. To obtain MHz chopped e-beam, a commercial pulse junction box (Kimball Physics part # 49-000040) was used to drive a pair of blanker plates inside the electron gun system. A function generator followed by a voltage amplifier (Tabor Electronics MODEL A10160) supplied a voltage of 10 - 34V on the deflector. However, the junction box and blanker is not compatible with 1-2GHz chopping frequency. A customer-made deflector was used to realize a GHz chopped e-beam (Figure 4.2). The deflector is simply a pair of single side PCB plates with a $10cm$ length and a $1cm$ width. The gap between the two electrostatic plates is $0.6cm$. A ROHDE SCHWARZ SMC 100A GHz function generator following with an OPHIR 5205 power amplifier was used to supply a harmonic wave of tens of volts on the deflector. A 50ohm resistor and a Screw Tuners(MODEL 1643N) are added in series with the plates for impedance matching. Without tuning, most of the forwarded power would be reflected back to the power amplifier.

We tried to use the same deflection setup to realize f and $2f$ chopping frequencies. A periodic voltage with frequency f was applied on the deflector, which deflect the e-beam spot to a line. When the e-beam line is placed at the edge of the passing hole, the e-beam is chopped with frequency f. Alternatively, the e-beam line can be placed across the passing hole as shown in Figure 4.3. Electrons sweep across the hole which produces a $2f$ chopping frequency. The

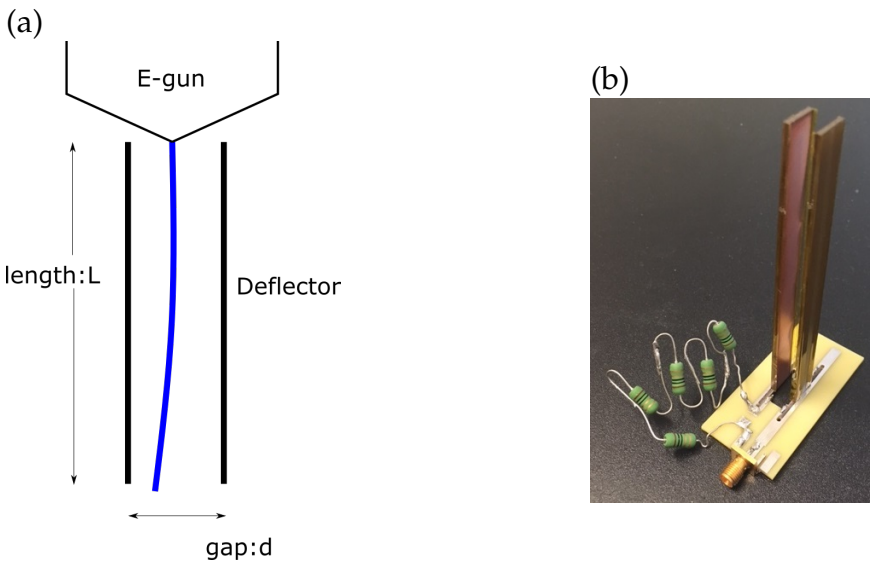

Figure 4.2: Deflector sketch(a) and picture(b).

$2f$ component was observed in experiments, but with a much smaller amplitude compared to the f chopping case. This was due to the deficient deflection length (Figure 4.3 Experiment case). If the e-beam size is focused to a sufficiently small diameter and the deflection length is large enough, a $2f$ chopping frequency should be easily realized.

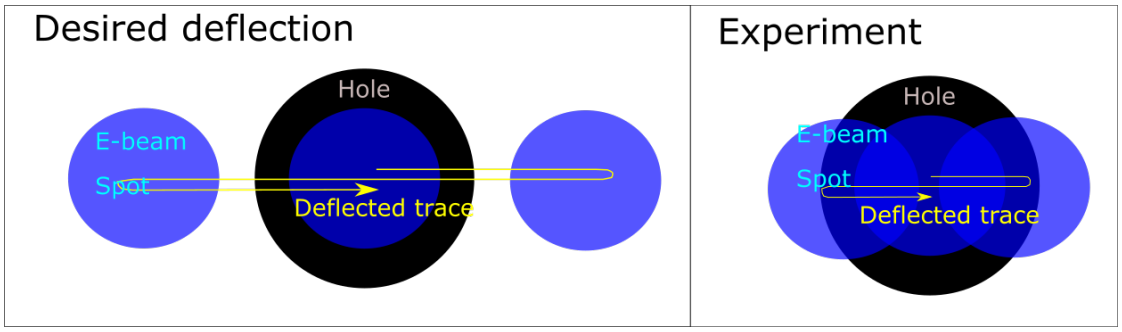

Figure 4.3: Concept of 2f chopping.

The e-beam was modulated at MHz and GHz. Both cases used a silicon chip as target specimen. The MHz acoustic wave was detected by a $4cm \times 4cm \times 0.5mm$

Table 4.1: Piezoelectric material parameters

Material	d_{33}	ϵ_r	g_{33}
PZT (APC840)	290 pC/N	1275	26.5 $\times 10^{-3} Vm/N$
Alumina-Nitride	5.5 pC/N	4.84	128$\times 10^{-3} Vm/N$

Lead zirconate titanate (PZT) transducer, which was glued to the rear side of a silicon chip with superglue (3M Scotch-Weld CA40). The GHz acoustic wave was picked up by a 0.5mm diameter, 2μm thick aluminum-nitride (AlN) transducer, which was fabricated at the Institute of Microelectronics. A summary of their elastic properties and piezoelectric parameters are listed in Table 4.1.

4.2 Results with PZT Transducers

The output from the PZT was fed into a customer-made TIA with a 20K feed-through resistor, and then connected to an Agilent Infiniium Oscilloscope 1$M\Omega$ port to display the signal.

The impedance frequency dependence was measured with an Impedance Analyzer (Figure 4.4), which shows two resonance frequencies at 3.85MHz and 4.56MHz. A Q factor of 6.05 was calculated from Eq. 3.8 given the resonant frequency and impedance values shown in Figure 4.4. The deposited power density is $\sim 10^6 W/m^2$ (Eq. 2.6). With a $\sim 5MHz$ chopping frequency, the stress launched at the PZT transducer is $\sim 0.2N/m^2$ (Eq. 2.28) and the output voltage from the TIA is estimated to be $\sim 7 \times 10^{-4} V \times Q_m = \sim 4 \times 10^{-3} V$ (Eq. 3.5 and Eq. 3.9).

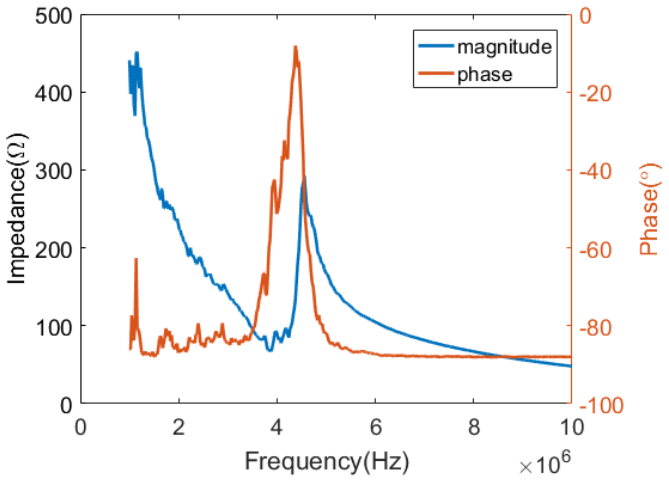

Figure 4.4: PZT impedance as a function of the driven frequency.

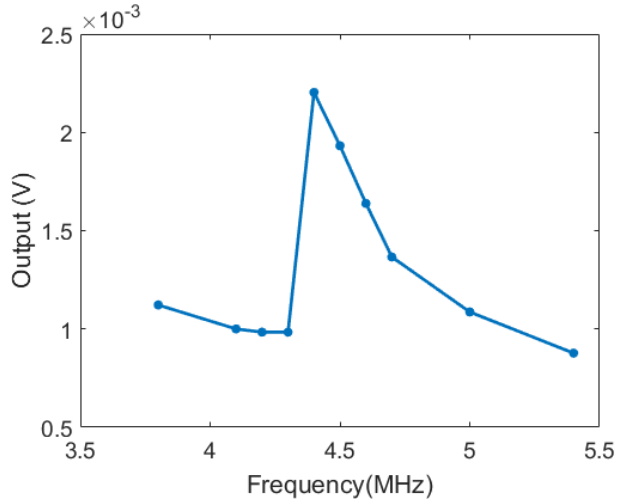

Figure 4.5: SEAM signal(from TIA) as a function of the chopping frequency.

Figure 4.5 displays the electron acoustic (EA) signal as a function of the chopping frequency. The EA signal behaves resonant at 4.4MHz, which corresponds to the resonance frequency f_m. Anti-resonance frequency f_n does not appear because the amplitude of the voltage drops below the noise level. The resonance frequency of the EA signal shows a shift compared to the one measured by the impedance analyzer (Figure 4.4), which is due to the parasitic capacitance

or inductance introduced by the wire connections, the piezoelectric impedance changes due to the temperature and pressure variations, or even the assembly of specimen on the XY stage. The amplitude of the EA signal is close to the estimated voltage $\sim 4mV$. The small decrement comes from the overestimation of the Q_m factor or extra resistances caused by the wire connections.

A pulse test was done on the electron acoustic signal with a PZT transducer. A pulse test applies a voltage pulse containing several wave cycles on the deflector, and consequently generates a pulsed e-beam. The time-varying e-beam generates an acoustic wave, which takes propagating time $t = \frac{specimen\ thickness}{longitudinal\ wave\ speed}$ to arrive at the transducer surface. Consequently, the EA signal displays a time delay compared to the triggering voltage. Pulse tests for PZT are relatively hard, because the MHz acoustic wave has a $\sim \mu s$ period, which is longer than the propagating delay time. In experiments, voltage with two cycles of a 4.5MHz wave was applied to minimize the overlap between electron acoustic signal and the voltage triggering signal. As can be seen from Figure 4.6, the PZT output shows a $\sim 106ns$ time delay compared to the input signal. The traveling time in the specimen is estimated to be $t = t_{silicon}/v_L = 59.3ns$, which agrees with the detected output response considering extra delay due to wire connections.

4.3 Results with AlN Transducers

The same e-beam energy and calculation steps were applied to the estimation of the GHz EA signal. The output voltage of the AlN transducer was calculated to be $\sim 10nV$ from Eq. 3.4. Because the size of the AlN pixels are much smaller than the PZT transducers, the signal amplitudes drop even when the frequency

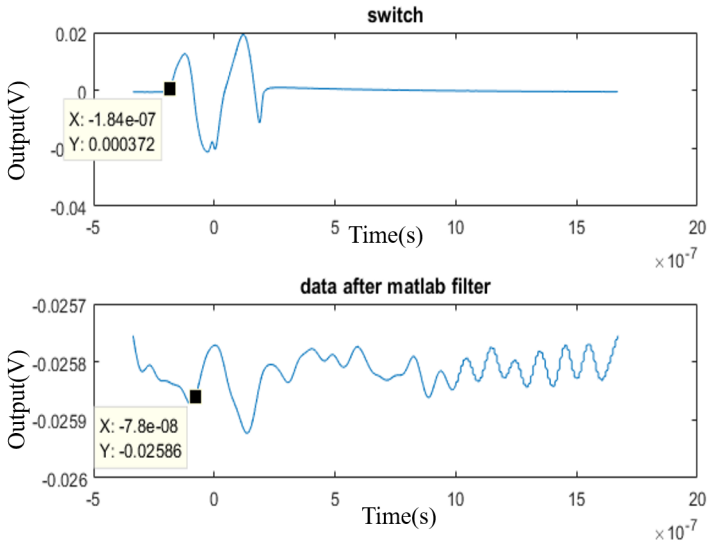

Figure 4.6: Pulse test on PZT.

increases. The output signal is amplified by a RedBox Amplifier, providing an 18dB gain (the TIA is not compatible with GHz frequency). The final signal amplitude is expected to be $\sim 80nV$, which is very small to capture. However, a lock-in amplifier might be able to capture it after further amplification. Scope used here is a LeCroy 8500A Wavemaster 5 GHz storage oscilloscope, which has a 5GHz bandwidth and 10GS/s sample rate.

Measurements from the AlN transducer in the time domain is displayed in Figure 4.7 , with a 1.5GHz chopping frequency. When the e-gun is off, the output still displays a harmonic wave oscillating at the chopping frequency, which comes from the RF radiation signal produced by the deflector. Figure 4.8 compares the output signals of a AlN pixel in the frequency domain with the e-gun on and off. As the e-beam energy increases, the signals with the e-gun on become slightly bigger than the cases where the e-gun is off. This increment is

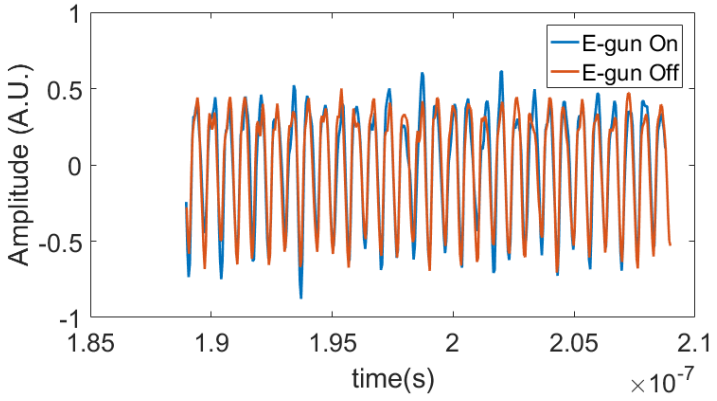

Figure 4.7: AlN output from a scope (E-beam energy 6keV).

caused by the increase of the acoustic wave amplitude as the e-beam energy rises. Further experiment modifications are needed to get rid of the RF coupling.

Several failed attempts were made to eliminate the RF impact. A Faraday cage was made to block the electromagnetic field (Figure. 4.9). The RF background was attenuated a little bit by the cage, but still showed a few mV amplitude. The failure might be due to an open slot used for wire connections. Another approach used two identical AlN pixels. One pixel was exposed to the chopped e-beam, while the other one was hidden away from the electrons. The RF coupling is expected to be canceled by subtracting signals from the two pixels. However, experimentally these two pixels cannot be exactly the same. It is hard to eliminate the differences in wire bonding connections and spatial positions. Figure 4.10 displays a pulse test done on the AlN pixels. The phase difference between two "identical" pixels has been removed by MATLAB. Several reflected wave packets are observed, but only some of them are due to the acoustic wave. The acoustic wave propagates through the specimen and arrives at the transducer surface with a delay time t, and consequently causes

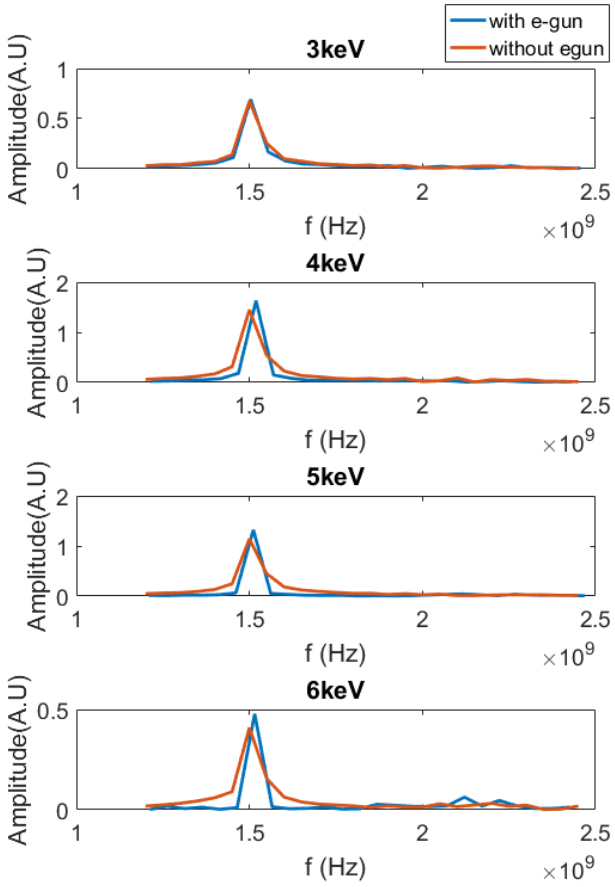

Figure 4.8: FFT plot of AlN output with electron gun on and off (Sampling frequency: 130GHz).

reflected waves at $3t$, $5t, \cdots$ While the electromagnetic wave travels to the AlN surface with the speed of light and excites the transducer almost instantly. This RF coupling generates reflected wave packets at time $2t$, $4t, \cdots$ The acoustic induced signal is expected to happen between RF coupling wave packet, which is shown in Figure 4.10. The amplitude of the acoustic wave is small and attenuates quickly. Further improvements are required in improving SNR.

Figure 4.9: Faraday cage.

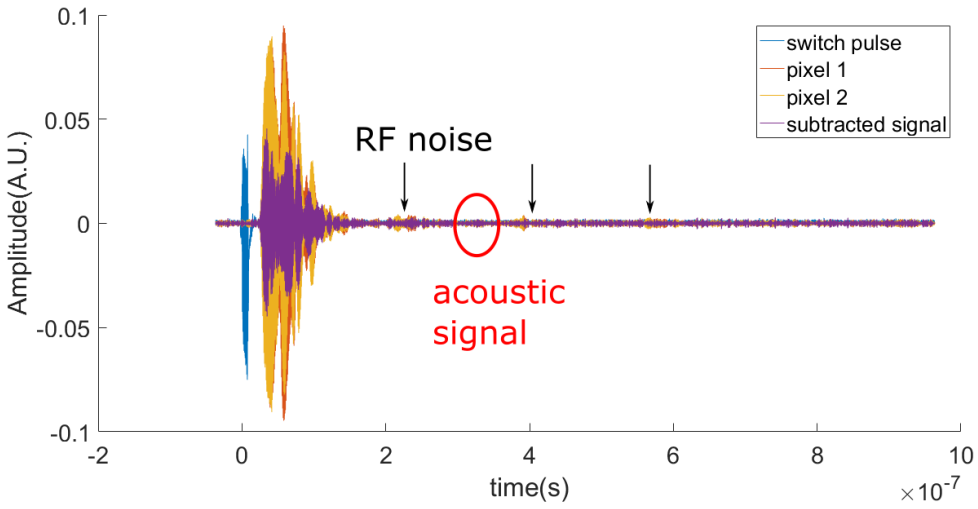

Figure 4.10: Subtracted Pixels Signal

CHAPTER 5

CONCLUSIONS AND FUTURE WORK

In this work, a detailed derivation of the heat induced acoustic wave generation, propagation and detection are given. The developed model demonstrates that the resolution of the SEAM signal mainly depends on the e-beam chopping frequency, electron energy, and the specimen thermal and elastic coefficients. It also shows that GHz-SEAM is capable of producing 10-100nm resolution images. In the experimental section, we display the results with an e-beam modulated at 4.5MHz and 1.3GHz. MHz EA signals were detected by PZT transducers, and are in a good agreement with the theoretical estimation. GHz acoustic waves were picked up by AlN pixel transducers. The GHz EA signals were detected, but suffered significantly from the RF coupling. Further experiment modifications are needed to improve the SNR and to eliminate the RF coupling. With the results of our experiment, we conclude that GHz-SEAM shows potential for nanoscale mechanical properties imaging and bio-mechanical cells imaging.

As covered in the previous chapter, future work involves improving the SNR. Possible approaches include: making GHz lock-in amplifiers, applying high gain GHz-TIA, and optimizing circuit design to reduce noise out of band. The realization of GHz-SEAM would provide a nanoscale, 3D imaging methods for understanding the mechanical properties of various materials.

BIBLIOGRAPHY

[1] G SIII Cargill. Ultrasonic imaging in scanning electron microscopy. *Nature*, 286(5774):691–693, 1980.

[2] Elmar Brandis and Allan Rosencwaig. Thermal-wave microscopy with electron beams. *Applied Physics Letters*, 37(1):98–100, 1980.

[3] Joseph Goldstein, Dale E Newbury, Patrick Echlin, David C Joy, Alton D Romig Jr, Charles E Lyman, Charles Fiori, and Eric Lifshin. *Scanning electron microscopy and X-ray microanalysis: a text for biologists, materials scientists, and geologists*. Springer Science & Business Media, 2012.

[4] Ludwig Josef Balk. Scanning electron acoustic microscopy. *Advances in Electronics and Electron physics*, 71:1–73, 1988.

[5] BT Khuri-Yakub. Scanning acoustic microscopy. *Ultrasonics*, 31(5):361–372, 1993.

[6] C Ilett, MG Somekh, and GAD Briggs. Acoustic microscopy of elastic discontinuities. In *Proceedings of the Royal Society of London A: Mathematical, Physical and Engineering Sciences*, volume 393, pages 171–183. The Royal Society, 1984.

[7] LJ Balk, DG Davies, and N Kultscher. The dependence of scanning electron acoustic microscopy (seam) imaging on chopping and detection frequency for metal samples. *physica status solidi (a)*, 82(1):23–33, 1984.

[8] M Urchulutegui, J Piqueras, and J Llopis. Scanning electron-acoustic microscopy of mgo crystals. *Journal of Applied Physics*, 65(7):2677–2680, 1989.

[9] DG Davies, A Howie, and L Staveley-Smith. Scanning electron acoustic microscopy. *SPIE MILESTONE SERIES MS*, 53:176–176, 1993.

[10] John H Cantrell, Menglu Qian, MV Ravichandran, and KM Knowles. Scanning electron acoustic microscopy of indentation-induced cracks and residual stresses in ceramics. *Applied physics letters*, 57(18):1870–1872, 1990.

[11] GS Cargill III and E Ash. Scanned image microscopy. *Academic Press (New York, 1980) pg*, 319, 1980.

[12] Allan Rosencwaig. Thermal-wave imaging. *Science*, 218(4569):223–228, 1982.

[13] DG Davies, RE Green, M Somekh, and G Busse. Scanning electron acoustic microscopy and its applications. *Philosophical Transactions of the Royal Society of London A: Mathematical, Physical and Engineering Sciences*, 320(1554):243–255, 1986.

[14] Mingyao Liu, A Keith Tanswell, and Martin Post. Mechanical force-induced signal transduction in lung cells. *American Journal of Physiology-Lung Cellular and Molecular Physiology*, 277(4):L667–L683, 1999.

[15] GEOFFREY Goldspink, ANDREW Scutt, PAUL T Loughna, DOMINIC J Wells, THOMAS Jaenicke, and GERALD F Gerlach. Gene expression in skeletal muscle in response to stretch and force generation. *American Journal of physiology-regulatory, integrative and comparative physiology*, 262(3):R356–R363, 1992.

[16] LV Harter, KA Hruska, and RL Duncan. Human osteoblast-like cells respond to mechanical strain with increased bone matrix protein production independent of hormonal regulation. *Endocrinology*, 136(2):528–535, 1995.

[17] J H-C Wang and B P Thampatty. An introductory review of cell mechanobiology. *Biomechanics and modeling in mechanobiology*, 5(1):1–16, 2006.

[18] Deok-Ho Kim, Pak Kin Wong, Jungyul Park, Andre Levchenko, and Yu Sun. Microengineered platforms for cell mechanobiology. *Annual review of biomedical engineering*, 11:203–233, 2009.

[19] Claudia Brunner, Axel Niendorf, and Josef A Käs. Passive and active single-cell biomechanics: a new perspective in cancer diagnosis. *Soft Matter*, 5(11):2171–2178, 2009.

[20] Manfred Radmacher. Measuring the elastic properties of biological samples with the afm. *IEEE Engineering in Medicine and Biology Magazine*, 16(2):47–57, 1997.

[21] Ming-Tzo Wei, Angela Zaorski, Huseyin C Yalcin, Jing Wang, Melissa Hallow, Samir N Ghadiali, Arthur Chiou, and H Daniel Ou-Yang. A comparative study of living cell micromechanical properties by oscillatory optical tweezers. *Optics express*, 16(12):8594–8603, 2008.

[22] Andreas R Bausch, Florian Ziemann, Alexei A Boulbitch, Ken Jacobson, and Erich Sackmann. Local measurements of viscoelastic parameters of adherent cell surfaces by magnetic bead microrheometry. *Biophysical journal*, 75(4):2038–2049, 1998.

[23] Gustavo Esteban-Manzanares, Blanca González-Bermúdez, Julia Cruces, Mónica De la Fuente, Qingxuan Li, Gustavo V Guinea, José Pérez-Rigueiro, Manuel Elices, and Gustavo R Plaza. Improved measurement of elastic properties of cells by micropipette aspiration and its application to lymphocytes. *Annals of biomedical engineering*, 45(5):1375–1385, 2017.

[24] C Ross Ethier and Craig A Simmons. *Introductory biomechanics: from cells to organisms*. Cambridge University Press, 2007.

[25] Niels De Jonge, Diana B Peckys, GJ Kremers, and DW Piston. Electron microscopy of whole cells in liquid with nanometer resolution. *Proceedings of the National Academy of Sciences*, 106(7):2159–2164, 2009.

[26] R Shimizu, T Ikuta, TE Everhart, and WJ DeVore. Experimental and theoretical study of energy dissipation profiles of kev electrons in polymethylmethacrylate. *Journal of Applied Physics*, 46(4):1581–1584, 1975.

[27] David C. Joy. Electron beam monte carlo simulator.

[28] Paul K Dixon and Sidney R Nagel. Frequency-dependent specific heat and thermal conductivity at the glass transition in o-terphenyl mixtures. *Physical review letters*, 61(3):341, 1988.

[29] Yee Kan Koh and David G Cahill. Frequency dependence of the thermal conductivity of semiconductor alloys. *Physical Review B*, 76(7):075207, 2007.

[30] Jim Wilson. Thermal diffusivity. *Electronics Cooling*, 13(3):7, 2007.

[31] Jürgen Blumm and André Lindemann. Characterization of the thermophysical properties of molten polymers and liquids using the flash technique. *High Temp. High Press*, 35(36):627, 2003.

[32] Richard M White. Generation of elastic waves by transient surface heating. *Journal of Applied Physics*, 34(12):3559–3567, 1963.

[33] Daniele Fournier, Claude Boccara, Andrew Skumanich, and Nabil M Amer.

Photothermal investigation of transport in semiconductors: Theory and experiment. *Journal of applied physics*, 59(3):787–795, 1986.

[34] Jacques Cazaux. Some considerations on the electric field induced in insulators by electron bombardment. *Journal of Applied Physics*, 59(5):1418–1430, 1986.

[35] George Brewer. *Electron-beam technology in microelectronic fabrication*. Elsevier, 2012.

[36] Boaz Nash. Physics of the electron beam source: beam size, shape and lifetime and the relationship to the xray radiation properties. Talk.

[37] H-J Hunger and L Küchler. Measurements of the electron backscattering coefficient for quantitative epma in the energy range of 4 to 40 kev. *physica status solidi (a)*, 56(1), 1979.

[38] Gordon SGS Kino. *Acoustic waves: devices, imaging and analog signal processing*. Number 43 KIN. 1987.

[39] NDT Resource Center. Introduction to ultrasonic testing.

[40] F Alan McDonald. Practical quantitative theory of photoacoustic pulse generation. *Applied Physics Letters*, 54(16):1504–1506, 1989.

[41] SO Reza Moheimani and Andrew J Fleming. Fundamentals of piezoelectricity. *Piezoelectric transducers for vibration control and damping*, pages 9–35, 2006.

[42] J Erhart, Petr Pulpan, and Martin Pustka. *Piezoelectric Ceramic Resonators*. Springer, 2017.

[43] Ltd APC International. *Piezoelectric ceramics: principles and applications*. APC International, 2002.

[44] L Balk, D Davies, and N Kultscher. Investigation of si-fe transformer sheets by scanning electron acoustic microscopy (seam). *IEEE transactions on magnetics*, 20(5):1466–1468, 1984.